

SUPPLEMENTARY METHODS

Growth of monolayer (ML) transition metal dichalcogenide (TMD) films. Wafer scale ML films of MoS₂, WS₂ and MoSe₂ were grown by metal organic chemical vapor deposition (MOCVD)²⁰. Molybdenum hexacarbonyl (MHC), tungsten hexacarbonyl (THC), diethyl sulfide (DES), and dimethyl selenide (DMSe) are selected as chemical precursors for Mo, W, S, and Se respectively, and introduced to a tube furnace in gas phase. H₂ and Ar are injected to the growth chamber using separate lines. The optimum growth parameters for ML TMD films are as follows. We use a total pressure of ~ 10 Torr, growth temperature of 550 °C and growth time of 26 hrs. The flow rates of precursors are 0.01 sccm for MHC or THC, 0.4 sccm for DES or DMSe, 5 sccm for H₂, and 150 sccm for Ar, which were regulated by individual mass flow controllers (MFCs). NaCl is loaded in the upstream region of the furnace, which increases the grain size and monolayer yield²⁰.

Programmed vacuum stack (PVS) process. *Fabrication of initial layer L0:* L0 is used as the stamp layer, which is generated as follows. Spin coating of an adhesive polymer layer of PMMA (Poly-methyl methacrylate, 495 K, 4% diluted in anisole) for 90 seconds at 4000 rpm on an as-grown ML TMD film sitting on its growth substrate (SiO₂/Si). Baking 10 mins at 180 °C using a hot plate, followed by attaching a thermal release tape (TRT) manufactured by Nitto-Denko (3195MS). TRT/PMMA/L0 is then separated from the SiO₂/Si substrate via mechanical peeling without the use of any chemicals or etchants, which keeps the bottom surface of L0 clean (see Movie S1). Other materials that can conformally coat the TMD surface can be used instead of PMMA; they include PECVD SiO₂, ALD HfO₂, CVD Si, e-beam evaporated Au, and other polymers. This process can be generally applied to various MOCVD grown ML TMD films, such as MoS₂, WS₂, and MoSe₂.

Stacking in vacuum: As shown in Fig. S13, we use a custom-designed vacuum stacking apparatus, consisting of a vacuum sealed box, a vacuum pump, a linear motion vacuum feedthrough, and a heating unit. The stacking process is done as the following: Mount TRT/PMMA/L0 on the top holder and put another as-grown ML film (L1 to-be) on the bottom stage of the vacuum box. Evacuate the chamber to less than 200 mTorr and heat the bottom stage to 150 °C. Lower the top holder to make a contact between L0 and L1/SiO₂/Si using the z-motion linear vacuum feedthrough. Keep them in contact for 10 mins. Lift the top holder with the stacked sample. After these steps, TRT/PMMA/L0 is attached to L1/SiO₂/Si, forming a pristine L0/L1 interface.

2nd Peel and vacuum stack (and repeat): To improve the yield of the mechanical peeling, the following steps are taken before the next ‘peel’ (step IV) process: 1) release the used TRT from PMMA/L0/L1/SiO₂/Si by heating it at 110 °C under ambient conditions; 2) anneal the sample at 180 °C for 10 min; 3) attach a new TRT on PMMA/L0/L1/SiO₂/Si. After replacing the new TRT, the bottom of the sample (i.e., Si side,) is attached onto a glass slide using a double-sided tape. The stacked film (TRT/PMMA/L0/L1) is separated from the substrate by mechanical peeling, during which L1 stays attached to L0 (see supplementary notes below). The vacuum stack and peel process can be thereafter repeated for L2, L3, L4, ... to generate a stacked film with a desired number of layers and stacked vertical composition.

Transfer and release: (i) supported film: The stacked film is transferred on any target substrate using vacuum stacking (step III). Afterwards, TRT is removed by heating the sample at 110 °C under ambient conditions. The PMMA on top of the stacked films can be removed by either high vacuum ($< 10^{-6}$ Torr) annealing at 325 °C for 3 hrs, or soaking the sample into acetone. Before soaking in acetone, the sample is annealed at 180 °C in ambient for 30 mins and cooled down to ensure the adhesion between the film and the substrate. **(ii) suspended freestanding film:** As shown in Fig. S3, a suspended PMMA/ stacked film is generated by first mechanically peeling it using a TRT with a hole in the middle, which has a diameter larger than the target frame. The suspended PMMA/ stacked film is then brought into contact with the target frame. The entire structure is gradually heated from room temperature to 180 °C before the film outside of the frame is cut away by a knife. Finally, the PMMA is removed by high vacuum ($< 10^{-6}$ Torr) annealing at 325 °C for 3 hrs.

Water delamination and transfer. As-grown TMD films can be delaminated from the growth substrate by simply dipping it into water²⁹ with no polymer support or chemical treatment (See Movie S2). This process also works for stacked films, such as the 4L-Mo/W/Mo/WS₂ superlattice films shown in Fig. 4c. The detached films can then be picked up and transferred to other substrates. This process provides a facile way to transfer stacked films onto unconventional substrates, such as polyethylene terephthalate (PET, see Fig. 4c inset) or human skin.

Conventional dry transfer method. Here we adopted the method reported in ref. 11, which is described as the following: (1) spin 4% 495 K PMMA in anisole on a MoS₂ at 2,000 rpm for 1 min. (2) bake at 180 °C for 1 min. (3) attach thermal release tape with a ~1 cm wide hole on a MoS₂/SiO₂/Si sample. (4) detach the MoS₂ from SiO₂ surface by floating TRT/PMMA/MoS₂/SiO₂/Si sample on the 1M KOH solution surface. (5) move the TRT/PMMA/MoS₂ to the surface of pure water after detached for 5 min. Repeat this step for 6 times to ensure the residues from KOH solution is removed. (6) pick up and blow dry the bottom surface with nitrogen. (7) transfer TRT/PMMA/MoS₂ onto another MoS₂/SiO₂/Si. The second piece needs to be smaller than the holes on the TRT so that only the PMMA/MoS₂ part is touching the next MoS₂. (8) bake it at 180 °C for 15 min to produce good adhesion. (9) cut the PMMA/MoS₂ from the TRT supporter. (10) lift off PMMA with acetone at ~50 °C for 30 min and rinse the substrate with IPA. (11) for stacking more than three layers, repeat the whole process but, in step 7, N_L-MoS₂/SiO₂/Si substrate is used instead of MoS₂/SiO₂/Si.

Scanning transmission electron microscopy (STEM) analysis. A cross section of the specimen was prepared by using a standard lift-out procedure in a dual-beam FEI Strata 400 focus ion beam system with a final milling at 2 keV from randomly selected regions on a large scale stacked film. Afterwards, the specimen was baked in an ultrahigh vacuum chamber at 130 °C for 8 hours to clean the specimen. After baking, the specimen was transferred to a Nion Ultra-STEM 100 operated at 60 keV. The imaging condition was similar to that in ref. 31. For annular dark field (ADF) STEM images, the beam convergence angle was ~35 mrad, with a probe current of ~70 pA. The acquisition time was 8 μs per frame and we sum 10 frames. The electron energy loss spectroscopy (EELS) were acquired with an energy dispersion of 0.25 eV/channel using a Gata

Page | 2

Quefina dual-EELS Spectrometer. A linear combination of power laws (LCPL) was used to fit and subtract the background. The EELS false-color composition maps were created by integrating the S-L_{2,3} edge, C-K edge, Mo-M_{4,5} edge and Si-L_{2,3} edge (for SiO₂). All EELS analysis was done with open-source Cornell Spectrum Imager software³².

X-ray diffraction (XRD) measurements. The θ - 2θ scan of XRD in Fig. 2d was measured using Rigaku SmartLab X-Ray Diffractometer (parallel beam mode, power: 40kV, 44mA). The beam size is roughly $0.5 \times 1 \text{ cm}^2$ on the sample surface, as measured by fluorescent plate.

Optical measurements. *Optical absorption:* Optical absorption measurements were performed using a DUV-Vis-NIR hyper-spectral microscope or a Shimadzu UV-Vis-NIR Spectrometer for local or global measurements, respectively. The spot size is $\sim 50 \mu\text{m}$ for the hyperspectral microscope, and $\sim 1 \text{ cm}$ for the Shimadzu Spectrometer, as schematically shown in Fig. S6 (drawn not to scale). Specimens are prepared on fused silica substrates. In order to measure the absorption of the sample, we first measure its contrast of transmitted light (δ_T), defined as $|I_v - I_s|/I_s$, where I_v is the intensity of the transmitted light through the sample and the substrate, and I_s is the intensity through the substrate alone. When an atomically thin layered material, the thickness of which is much smaller than the wavelength of the incoming light, is placed on a thick, transparent substrate ($500 \mu\text{m}$ fused silica here), δ_T is directly related to the absorption of the sample (A) through $\delta_T = 2A/(n_s + 1)$ under thin-film approximation, where n_s is the refractive index of fused silica.

Raman spectroscopy/mapping: Measurements are performed using InVia Confocal Raman microscope (Renishaw) with a green laser (532 nm) for Fig. S4f (right column), and Horiba LabRAM HR Evolution NIR confocal Raman microscope with green laser (532 nm, the rest of Fig. S4 and S5). The laser spot size is $\sim 1 \mu\text{m}$. The samples are prepared on a SiO₂/Si substrate. All experiments are performed at room temperature.

Measurement for wavelength-sensitive optical windows: The optical microscope images in Fig. 4a are taken using an Olympus BX41 optical microscope with a 4x objective (NA= 0.10) equipped with white light illumination source. To select the photon energy of the illumination light, we use bandpass filters for green ($535 \pm 50 \text{ nm}$, 2.32eV) and near infrared ($800 \pm 10 \text{ nm}$, 1.55eV) wavelength. The vertical distance between 7L-MoS₂ window and the surface of gold reflectors is $\sim 200 \mu\text{m}$. The images are taken in the reflection mode.

Device fabrication. We start with an e-beam evaporation of Ti (5 nm)/Au (40 nm) on fused silica chips ($1.2 \times 1.2 \text{ cm}^2$). The bottom electrodes are patterned by defining an etch mask using standard photolithography (PL) method, followed by wet gold etching (Gold Etchants TFA, Transene). In order to have good contact with the stacked films, the bottom electrodes were carefully cleaned: After dissolving the photoresist (PR) in Microposit Remover 1165, we treat the substrate with O₂ plasma at 400W for 3 minutes in Glen 1000 resist strip system. A film (typically $\sim 5 \times 5 \text{ mm}^2$) with stacked N_L and vertical composition is then transferred to the bottom electrode via vacuum stacking (step III) described above, and the PMMA layer is removed in acetone. After the PMMA layer is removed, the initial layer L_0 is always more n-doped than the as-grown MoS₂. Therefore, we perform the super-acid treatment³³ on the devices to eliminate the doping from PMMA before

fabricating top electrodes. Afterwards, top electrodes are fabricated by e-beam evaporation of 40 nm Au, patterned by PL, wet gold etching, and removal of PR. During this Au etching step, the bottom Au electrodes are not affected because they are covered and protected by the film. In the next step, we remove the film outside the device area by defining an etch mask using PL and applying SF₆/O₂ plasma in an Oxford Plasma lab 80+ reactive ion etcher. In the final step, the super-acid treatment is performed again.

Electrical measurements. All the electrical measurements are performed in ambient conditions at room temperature with Karl Suss PSM6 probe station using tungsten probe tips (SE-20TB, Signatone). For J-V characterization, the probe station is coupled to source measurement units (Keithley 236 Source Measurement Units), voltage source (Keithley 213 Quad Voltage Source) and trigger (Keithley 2361 Trigger Controller). The J-V measurements on tunnel devices (Fig. 3) are performed in a four-probe geometry. For capacitance measurements, the probe station is coupled to a Keithley C-V system (Keithley 590 CV Analyzer/230 Programmable Voltage Source/5951 Remote Input Coupler). The capacitance measurements are conducted in two probe geometry, with a 15 mV excitation voltage at 100 kHz, and the parasitic capacitance of the instrument is measured and subtracted from the device values.

SUPPLEMENTARY NOTES

Below we present additional characterizations on the uniformity and interlayer quality (A. & Additional Data (AD) 1-5) and the interlayer coupling (B. & AD 6-7) to further support the central claim of our manuscript: wafer-scale high-quality heterostructure 2D films with pristine interfaces. To present these additional data in an organized way, we provide a table of contents below:

Table of Contents

A. Spatial uniformity and pristine interlayer interfaces on the large scale	4
<i>AD 1. High spatial yield and uniformity of PVS process</i>	
<i>AD 2. Layer dependent Raman mapping</i>	
<i>AD 3. Optical absorption spectroscopy for large-scale uniformity</i>	
<i>AD 4. Dark-field optical microscopy for surface flatness characterization</i>	
<i>AD 5. Larger-scale atomic force microscopy image (50 × 50 μm²)</i>	
B. Interlayer coupling	6
<i>AD 6. Photoluminescence study on the interlayer coupling in WS₂-WS₂</i>	
<i>AD 7. Photoluminescence and indirect bandgap in MoS₂-MoS₂</i>	
C. Additional notes	7

A. Spatial uniformity and pristine interlayer interfaces on the large scale

The central claim in this work is that PVS process offers wafer-scale fabrication of vertically-designed stacked films with excellent structural and interface quality down to sub-nanometer scale.

Characterizing these, therefore, would require a technique that covers the entire spectrum over 8-orders of magnitude of differing length scales (*i.e.*, having sub-nanometer resolution with centimeter field of view), which no single technique can provide. For example, the resolution of large-scale optical measurements is fundamentally limited by diffraction, while sub-nm scale high-resolution measurements such as STEM require ~ 10 billion images for 1 cm^2 sampling area, which is not practical. In order to meet this unique challenge in our experiment, we are using multiple advanced characterization techniques as described in the main text and Supplementary Table. I. Altogether, these data support both of our central claims, *i.e.*, spatial uniformity and pristine interlayer interfaces on the large scale.

AD 1. High spatial yield and uniformity of PVS process

In our PVS process, each monolayer film is completely separated from the growth substrate and transferred to the stacked film, which directly results in the wafer-scale uniformity of our stacked films. We confirm this perfect yield of the peel-and-stack process using SEM imaging and Raman mapping as shown in Fig S4, where the measurements were taken on five substrates after as-grown MoS₂ monolayers on each substrate were sequentially peeled and stacked to generate a 5L-MoS₂ film.

We first show the SEM images (Fig. S4b, c) and Raman E_{2g}¹ peak area mapping (40 by 40 μm , Fig. S4d, e) taken on an as-grown 1L-MoS₂ on SiO₂/Si substrate and the same substrate after the MoS₂ is successfully delaminated to generate L0 (Raman spectra in Fig. 4a). We found no MoS₂ residue after peeling, which confirms the perfect yield of our process (insets of c and e show results after a failed peeling shown for comparison). Fig. S4f shows a series of similar SEM images, Raman mapping and Raman spectra taken at five random locations of the substrates after L1 is separated using L0, L2 separated using L1, *etc.* No MoS₂ residues are observed in any of the measurements, suggesting a perfect peeling yield regardless of the number of repeated peeling and stacking.

AD 2. Layer dependent Raman mapping

Fig. S5a shows the Raman spectra measured from 1L-, 2L- and 5L-MoS₂ films generated using our PVS process. As in previous reports^{16,34,35}, we observed that the E_{2g}¹ (A_{1g}) peak shifts to a lower (higher) energy with the distance between E_{2g}¹ and A_{1g} peaks (Δ_{E-A}) increasing for a larger N_L . We measure $\Delta_{E-A} \sim 20 \text{ cm}^{-1}$ for monolayer and $\sim 22 \text{ cm}^{-1}$ for 2L-MoS₂, which is quantitatively consistent with the previous reports on twisted bilayer MoS₂.

Fig. S5b and c present the Raman mapping (40 by 40 μm) of E_{2g}¹ peak frequency measured over 1L-, 2L- and 5L-MoS₂ films, which show uniform peak positions for each area, confirming the spatial uniformity and expected layer number dependence of our films. Other mappings done with A_{1g} peak, as well as the peak intensity and width for either peaks, all show similar spatial uniformity (not shown). These Raman mapping images thus provide an evidence for the uniformity of our PVS films over tens of micron scale with submicron resolution.

AD 3. Optical absorption spectroscopy for large-scale uniformity

Fig. S6a presents spectra of PVS-stacked 10L-MoS₂ films measured at random locations (local 1-3) with spot size $\sim 50 \mu\text{m}$ and a spectrum measured using $\sim 1 \text{ cm}$ spot size (global). We observed

no significant difference between different locations or different characterization scale, suggesting that the film is spatially uniform over centimetre area at a resolution of tens of micrometers. Furthermore, the layer-dependent absorption follows the expected trend of $1-T^{N_L}$ with $T = 0.91$ at 532 nm, close to the reported value for ML MoS₂³⁶, indicating that the optical properties of the films are preserved during the transfer process regardless the number of stacking on the films. Together with the Raman mapping measurements above (sub-nanometer resolution over tens of micrometer), our data suggest that our stacked film is spatially uniform from submicron up to centimetre scale.

AD 4. Dark-field optical microscopy for surface flatness characterization

Nonideal interfaces in stacked TMD films, including bubbles and wrinkles, would result in enhanced light scattering (see Fig S7a). We use this effect to characterize the spatial density of scatterers in our films. In Fig. S7, we show the representative dark-field (DF) optical microscope images (75 by 100 μm) taken from two different 2L-MoS₂ films each generated by PVS process (Fig S7d) and conventional dry transfer method (Fig S7c). While both films show clear surfaces under bright field images (Fig S7b), the DF images show that there are significantly fewer scatterers (>99% reduction) in the film stacked using the PVS process (1k vs 161k scatterers per 1 mm²).

Using a similar procedure, we took thirty DF images equally spaced over $\sim 5 \times 5 \text{ mm}^2$ sample area and count the number of scatterers in each image. The spatial map of number of scatterers is shown for each sample in Fig. S7e and f. They show that the films stacked using PVS (Fig S7f) has significantly fewer scatterers (98% reduction on average), with only 1 scatterer observed over 20 by 20 μm area on average. This suggests much better interlayer interfaces in the films stacked using PVS process over a large scale.

AD 5. Large scale atomic force microscopy images (50 \times 50 μm^2)

Fig. S8a presents a large scale (50 \times 50 μm^2) AFM topography image taken from a 2L-MoS₂ film generated using PVS. It is flat and mostly featureless, which is consistent with the data shown in Fig. 2c of our original manuscript (2 \times 2 μm^2) as well as the DF optical characterization over larger 5 \times 5 mm² (AD 4 above). In contrast, the AFM image taken from another 2L-MoS₂ film stacked in air (Fig. S8b) shows a much rougher surface with significant fluctuations in its morphology, again consistent with the small-scale AFM image (showing bubbles and wrinkles) and larger scale DF optical images (increased number of optical scatterers).

Altogether, our XRD (Fig. 2d), DF optical (Fig. S7), and AFM images (Fig. 2e and S8) strongly suggest that the PVS films have excellent interlayer structure and pristine interlayer interfaces on the large scale. The high-quality interfaces lead to the uniform interlayer coupling in the films as discussed below.

B. Interlayer coupling

Our additional data (AD 6 & 7) show that there is indeed strong interlayer coupling in our stacked films. Our results of photoluminescence spectroscopy and imaging suggest that the interlayer coupling is spatially uniform and present in different TMD films.

AD 6. Photoluminescence study on the interlayer coupling in WS₂-WS₂

Fig. S9 first demonstrate the interlayer coupling in 2L-WS₂ (optical image in Fig. S9a) generated using PVS process with MOVCD-grown monolayer flakes. Fig. S9b (main panel) shows that the PL measured from a 2L-region is strongly quenched compared to the PL from a monolayer region. The bilayer PL spectra also show two additional peaks (see inset) that correspond to the indirect peak (peak I) and interlayer exciton peak (peak A_I)³⁷. The PL quenching and the presence of I peak indicate the direct-to-indirect bandgap transition due to the interlayer coupling in WS₂. In addition, Fig. S9c schematically illustrates the origin of the A_I peak, which occurs when A exciton is generated across different layers of twisted 2L-WS₂.

Fig. S9d further plots the PL spectra measured from multiple 2L-WS₂ samples with different interlayer rotation angles. The peak line-shape analysis is used to investigate the angle-dependence of I, A, and A_I peak energies, as shown in Fig. S9e (left). The results are in excellent agreement with the published results taken from as-grown twisted bilayer WS₂ reported in ref. 37 (duplicated in Fig. S9e (right)). This confirms the presence of strong interlayer coupling at the WS₂-WS₂ interfaces generated using PVS process.

AD 7. Photoluminescence study and indirect bandgap in MoS₂-MoS₂

Fig. S10 presents the PL study conducted on MoS₂-MoS₂ interfaces in a continuous 2L-MoS₂ film generated using our PVS process. Fig. S10a and b each show the optical reflection and the PL image of the MoS₂ film at the 1L/2L boundary. The PL image confirms that PL is quenched uniformly over the 2L-region (lower half; dark) as expected from the bilayer region. The comparison of the PL spectra taken over 1L vs 2L regions (Fig. S10c) shows that the PL intensity in the 2L region is reduced ~120 times. Moreover, the normalized PL spectrum (Fig. S10d) shows an indirect gap peak at around ~1.65 eV, consistent with the reported value for twisted bilayer MoS₂^{16,34}. These results again confirm the strong and uniform interlayer coupling in our 2L-MoS₂ film generated using PVS process.

In the above studies, we note that our samples show strong interlayer coupling without undergoing an annealing step under vacuum or H₂/Ar, as done in many previous reports using samples generated using conventional wet or dry transfer techniques for stacking^{17,38,39}. This offers another evidence that the interlayer quality is greatly improved when the films are generated using PVS process.

C. Additional notes

Mechanical peeling and water delamination of ML TMD films from the SiO₂/Si substrates. In our experiments, we observe that well-grown and high quality TMD films are easily detached from the growth substrate by our mechanical peeling and water delamination process with a nearly perfect yield, as shown in Fig. S4. This strongly suggests that TMD-TMD van der Waals interactions are stronger than TMD-SiO₂ interaction. However, we observe that the yield of mechanical peeling and water delamination is significantly lower for the following types of non-ideal samples: (1) oxidized TMD films, (2) off-stoichiometric films, for example, grown with high concentration of sulfur vacancies, and (3) carbon contaminated films. We ascribe this to the strong

binding between these active sites in the film and the substrate, whose interaction may be stronger than TMD-TMD van der Waals interaction. See Fig. S4 for comparison.

X-ray diffraction measurement for PVS-stacked MoS₂. As compared to single crystal bulk MoS₂, the peak observed from our PVS-stacked 4L-MoS₂ in Fig. 2d shows two different features: first, the peak location is shifted to a lower 2θ (~13.8° v.s. 14.4° for bulk). Second, the peak is broadened. For the peak shift, it suggests that the interlayer spacing in our films is larger than that in bulk MoS₂ (0.64 nm v.s. 0.62 nm). This different interlayer spacing is consistent with the theoretical predicted values for MoS₂ with interlayer rotations (0.65nm) and aligned lattice (0.62nm)¹⁶, respectively. The peak broadening, on the other hand, is commonly observed from thin films with greatly reduced thickness such as the 4L-MoS₂ here (~2.6 nm). However, we cannot exclude the effect from other factors such as the polycrystallinity and strain in our films, as well as the divergence of X-ray source due to the use of parallel beam mode.

Statistical analysis for zero-bias resistance-area product. In Fig. 3e, ten devices for each data point are randomly picked at different locations from the device array of each stacked film. To avoid over-weighting the outlier data points originating from the exponential dependence, all the statistical analysis and fitting are carried out by first converting the resistance data into a log scale. To convert the standard deviation of results from the $N_L=7$ device array into a thickness variation, we first calculate the geometric average value R_0A and the standard deviation δR_0A . Since R_0A increases by ~ 10 times with one additional layer, R_0A in log scale is approximately linearly proportional to N_L with slope ~ 1 in this regime. Therefore, we can calculate thickness variation by $\Delta N_L = \Delta(\log(R_0A)) = \log(R_0A + \delta R_0A) - \log(R_0A) = \log(1 + \delta R_0A/R_0A)$. This yields ~ 70 pm thickness variation over the 2×3 mm² area in Fig. 3e, assuming each MoS₂ layer is roughly 0.7 nm thick.

The tunnel model. The zero-bias resistance (R_0A , in $\Omega \cdot \mu\text{m}^2$) in our experiment is measured by linearly fitting each J-V curve within a small bias range (between ±10 mV). From the tunnel model in ref. 24, R_0A for MoS₂ can be described as:

$$R_0 \cdot A = \frac{h^2 N t_{\text{MoS}_2}}{e^2 \sqrt{2m\phi_B}} \exp\left(-\frac{4\pi\sqrt{2m\phi_B} N t_{\text{MoS}_2}}{h}\right), \text{ for } |eV| \ll \phi_B,$$

where h is the Planck constant, e and m electron charge and effective mass, t the thickness and ϕ_B the average height of the barrier. This equation shows that R_0A is independent of a small applied bias V , while exponentially dependent on parameters such as the barrier width and height. The exponential sensitivity therefore provides a good method to confirm the quality of our stacked films as tunnel barriers. In Fig. 3d, the dashed line comes from the above equation with parameters of ML MoS₂ ($t = 0.65$ nm, $m = 0.35m_0$ (m_0 the electron's free mass)) plus a single fitting parameter ϕ_B . When $\phi_B = 0.5$ eV, the equation shows the best fit as plotted. In comparison, the theoretical value of ϕ_B is ~ 0.8 eV for ML MoS₂ and ~ 0.4 eV for bulk MoS₂, according to the band alignment (work function of gold = 5.1 eV, conduction band edge of ML MoS₂ ~ 4.3 eV and bulk MoS₂ ~ 4.7 eV)^{25,40}. A single value of $\phi_B = 0.5$ eV provides an excellent fit to all our data from devices with different N_L 's even when we use the same effective mass for all samples; this estimated ϕ_B

Table I | List of our combined characterizations and their length scales. Here, the left end of each bar indicates the resolution of the technique, and the right end indicates the largest field of view.

SUPPLEMENTARY FIGURES

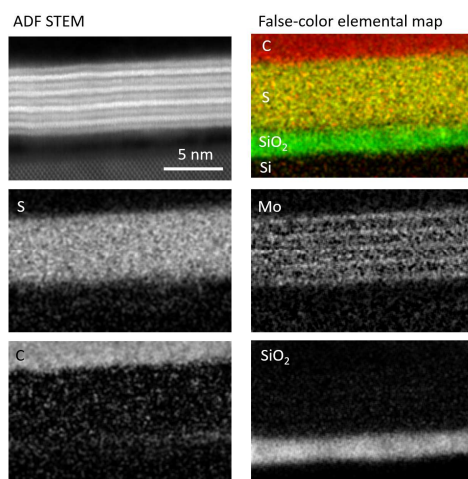


Fig. S1 | EELS spatial mapping corresponding to the ADF STEM image in Fig. 1.

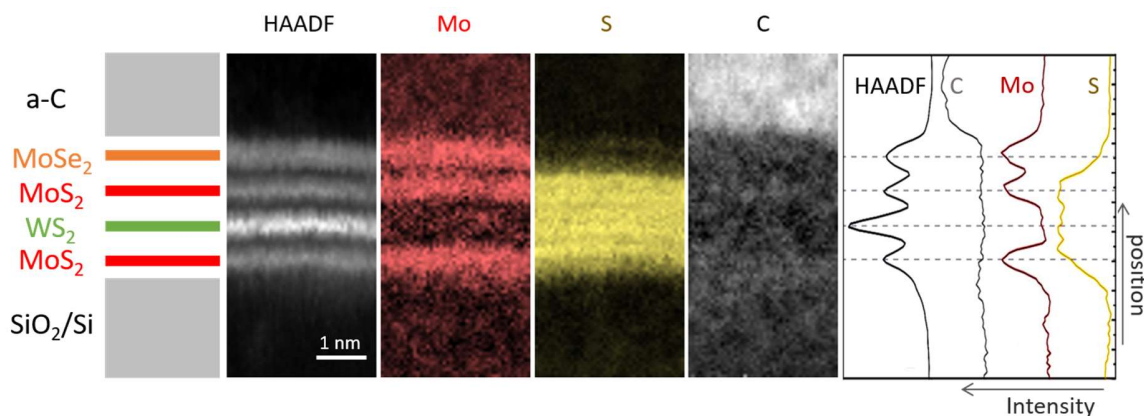


Fig. S2 | Vertically-designed film MoSe₂/MoS₂/WS₂/MoS₂ on a SiO₂/Si substrate. Similar to Fig.1, the ADF STEM image shows one bright layer for WS₂ and three darker layers for both MoSe₂ and MoS₂. EELS mapping further confirms that Mo signal only appears for MoSe₂ and MoS₂ layers, and S only in WS₂ and MoS₂. Carbon signal is again very low within the film, near the detection limit of our instrument.

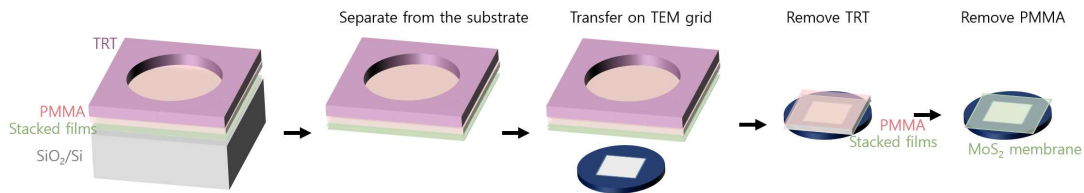


Fig. S3 | Schematics of the transfer process for generating large-scale freestanding films. See Method for detail description of the steps.

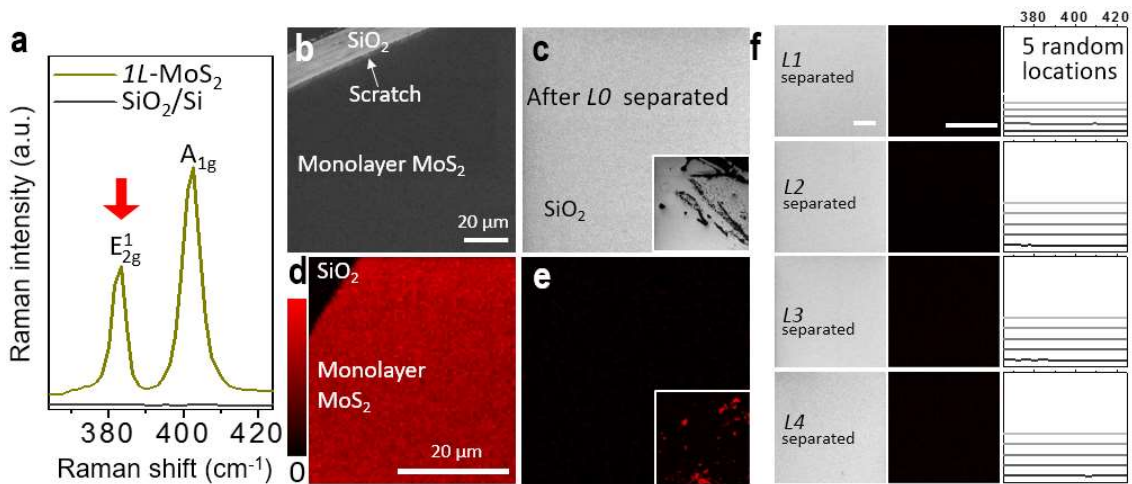


Fig. S4 | High yield of mechanical peeling. **a**, Raman spectra taken on SiO₂/Si substrates with (dark yellow) and without (grey) as-grown 1L-MoS₂. The E_{2g}¹ peak (indicated by a red arrow) is used for Raman mapping below. **b**, **c**, SEM images of 1L-MoS₂ and a substrate after the MoS₂ is successfully separated. Left-top scratch in **b** is made intentionally to expose SiO₂ for contrast. Inset of **c**: an example of failed peeling when low quality MoS₂ is used. **d**, **e**, Raman peak area mapping around the E_{2g}¹ peak frequency in correspondence to the SEM in **b** and **c**; inset of **e** for failed peeling. **f**, SEM (left column), Raman E_{2g}¹ peak area mapping (middle) and Raman spectra from five random locations (right column) taken on a series of substrates after additional peeling steps (generating L1, L2, L3 and L4). No MoS₂ residues are observed in any of the images, indicating a nearly perfect peeling yield regardless of the number of repeated peeling and stacking. Scale bars: 20 μm.

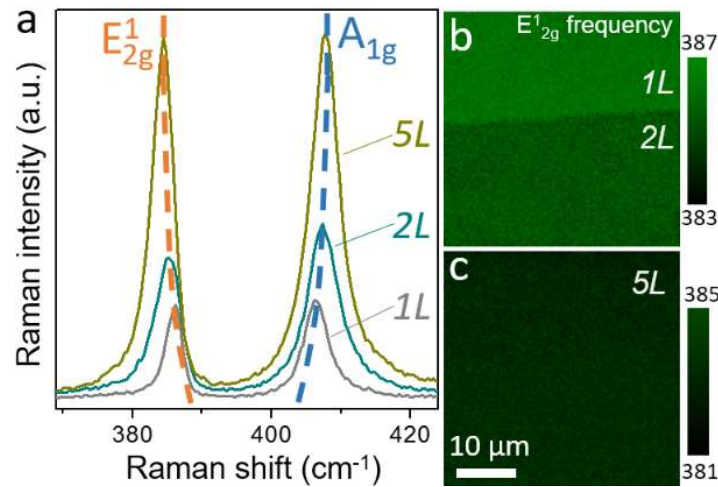


Fig. S5 | Uniform Raman properties of PVS-stacked MoS₂ films. **a**, Raman spectra taken from 1L-, 2L- and 5L-MoS₂. Dashed lines track the trajectory of peak frequency as a function of N_L . **b**, Raman frequency mapping of E¹_{2g} peak across 1L- and 2L-MoS₂ films. **c**, Raman frequency mapping of E¹_{2g} peak at 5L-MoS₂. All regions show uniform and consistent Raman properties.

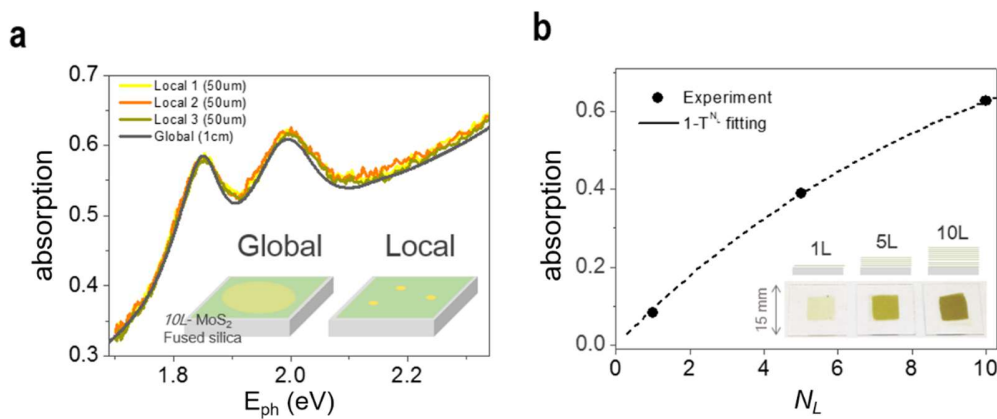


Fig. S6 | Optical absorption spectra of N_L -MoS₂ films. **a**, spectra of 10L-MoS₂ measured at three random locations (local 1-3) with spot size $\sim 50 \mu\text{m}$, compared to spectrum using $\sim 1 \text{ cm}$ spot size (labelled as ‘global’). All spectra are similar, indicating the film has spatially uniform properties. Inset: schematics of the sample and the measurements. (spots not drawn to scale) **b**, absorption measured at 532 nm as a function of N_L using 1cm spot size. The trend follows the expected layer dependent absorption $1-T^{N_L}$ with $T = 0.91$, close to the value for ML MoS₂. Inset: Schematics and photos of the measured films, $N_L=1, 5, 10$.

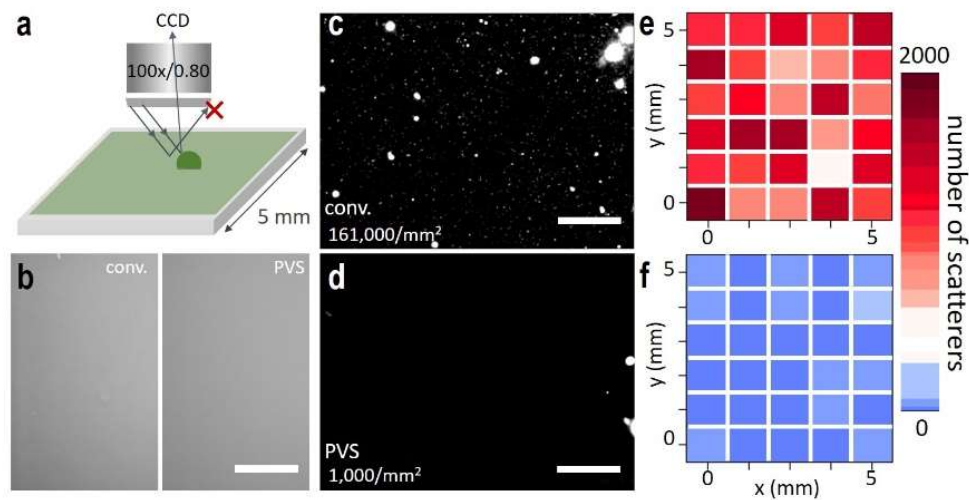


Fig. S7 | Dark-field optical microscope imaging of $2L$ - MoS_2 generated by conventional dry transfer (c and e) and PVS (d and f) method. **a**, a schematic of the experimental set-up. **b**, bright field microscope images. **c** and **d**, representative dark-field images of each sample. **e** and **f**, scatterer number maps generated using thirty DF images taken over $5 \times 5 \text{ mm}^2$ sample area. Scale bars: $20 \mu\text{m}$.

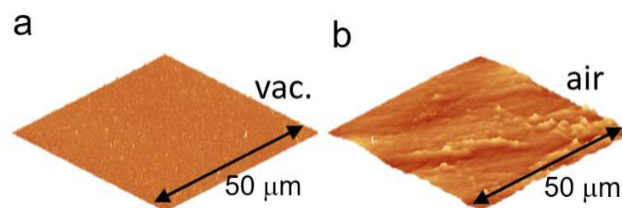


Fig. S8 | Additional $50 \times 50 \mu\text{m}^2$ AFM images taken from the bottom side of $2L$ - MoS_2 films stacked **a**, in vacuum and **b**, in air. The height scale is $\pm 25 \text{ nm}$.

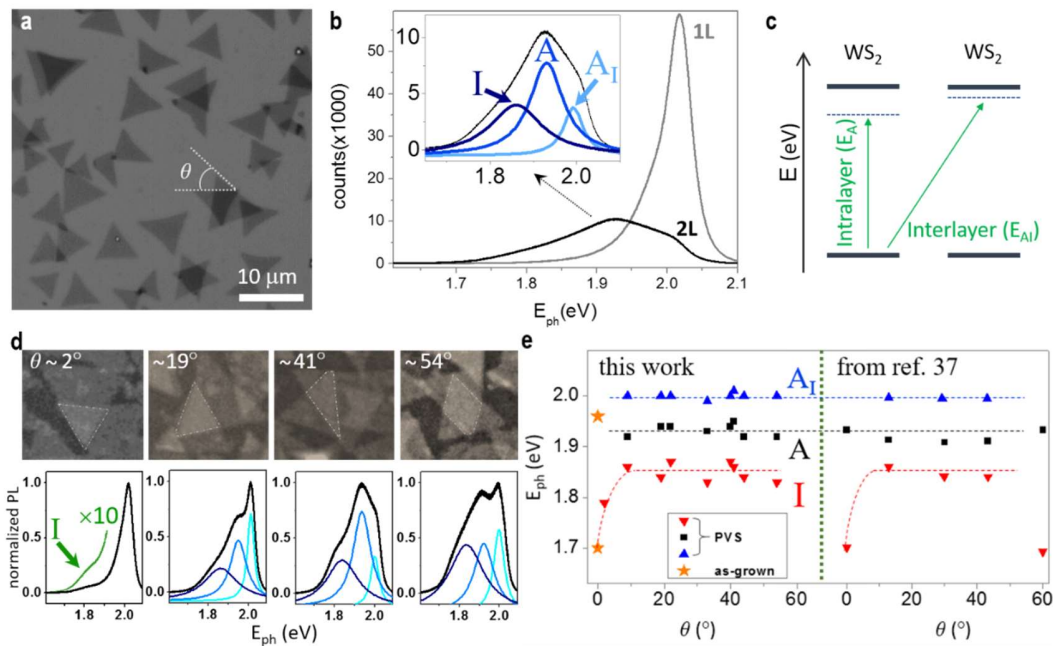


Fig. S9 | Interlayer coupling in PVS-stacked bilayer WS_2 . **a**, optical image of the sample. We approximate the twist angle using the edge orientation of each layer. **b**, PL spectra of $1L$ - and $2L$ - WS_2 . Inset: zoom-in of the spectrum for $2L$ - WS_2 . The peak can be fitted by three peaks: indirect transition peak I, direct transition peak of intralayer exciton (A) and direct transition of interlayer exciton peak (A_1). **c**, schematics of the transitions for intralayer and interlayer A excitons of WS_2 . **d**, optical images and PL spectra of $2L$ - WS_2 regions with different twist angles. **e**, angle-dependence of (left) PVS-stacked WS_2 compared to (right) those reported in ref. 37.

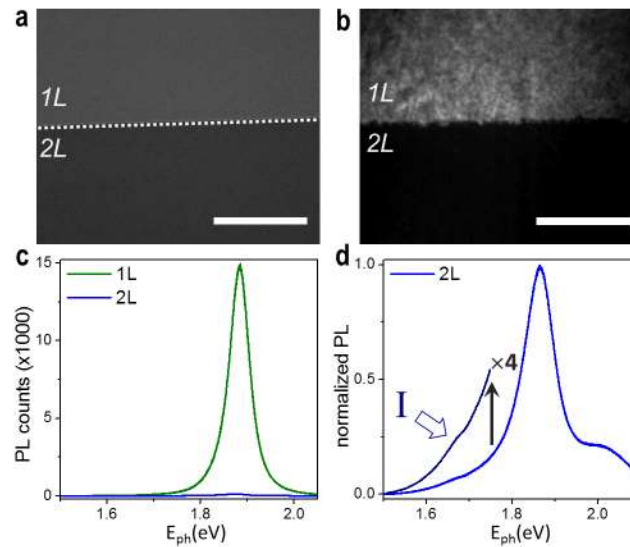


Fig. S10 | Uniform interlayer coupling in vacuum-stacked bilayer MoS₂. **a**, an optical microscope image at the *1L/2L* junction. **b**, PL image at the same location shows strong, uniform PL quenching in the *2L*-region (dark, lower part). Scale bars: 20 μm . **c**, PL spectra from both regions show a ~ 120 times quenching in *2L*-MoS₂ compared to *1L*. **d**, normalized PL spectrum from *2L*-MoS₂. We multiply the spectrum around 1.65 eV by four times to show the weak indirect gap PL peak.

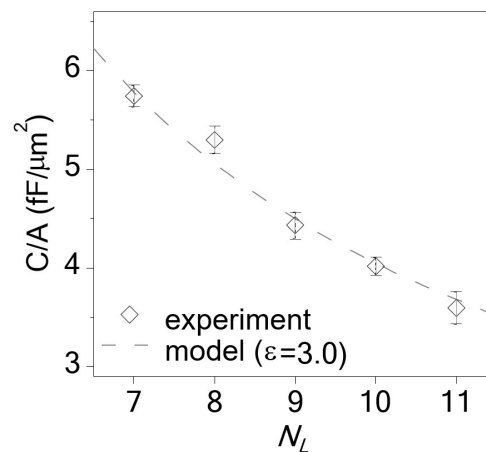


Fig. S11 | Capacitance per unit area versus N_L . Each data point is the average of ten devices. The dashed line is calculated for a parallel plate capacitor with a dielectric constant $\epsilon = 3.0$. The error bars are the standard deviation.

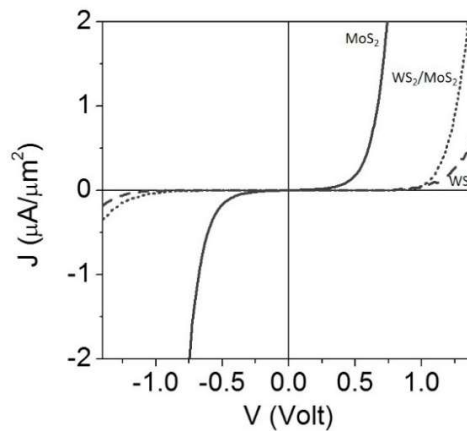


Fig. S12 | J-V curves of 6L-MoS₂, 6L-WS₂ and WS₂(3L)/MoS₂(3L) devices at large bias regime. For MoS₂ device, the J-V curve is symmetric for the entire V range. For WS₂, it is generally symmetric, with only a small bias-dependence asymmetry ($|I(\text{forward})/I(\text{reverse})| < 2$ at $V = \pm 1.4$). In contrast, the WS₂/MoS₂ device displays a much larger asymmetry ratio $|I(\text{forward})/I(\text{reverse})| > 10$ at $V = \pm 1.4$.

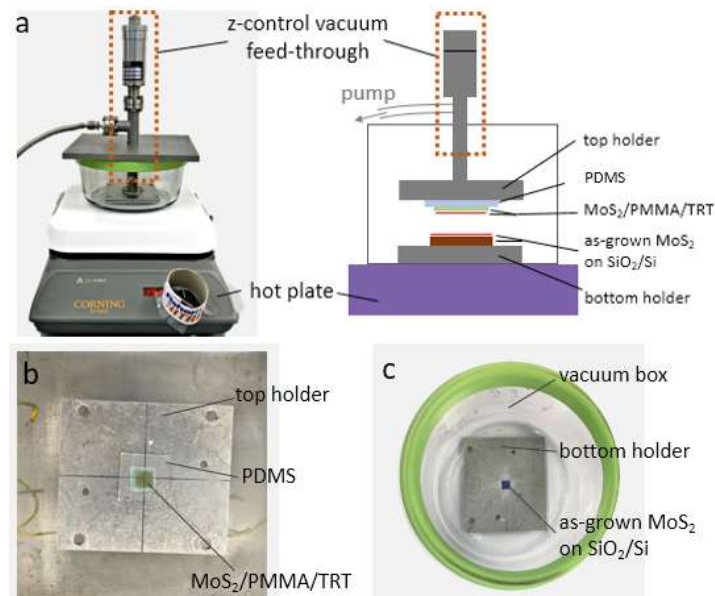


Fig. S13 | Details of the vacuum-stacking apparatus. **a**, (left) a photo of the vacuum stacking setup. (right) a schematic illustrating each component. **b**, a photo of the top holder used to hold the PVS-stacked MoS₂. The MoS₂/PMMA/TRT is held by a PDMS. **c**, a top-view photo of the vacuum-box with the bottom holder. An as-grown monolayer MoS₂ on SiO₂/Si is simply placed on top of the bottom holder.

Video S1 | Mechanical peeling of a 5 cm ML MoS₂ film with *TRT*/PMMA from its growth substrate (SiO₂/Si in our experiment).

Video S2 | Delamination process of a ML MoS₂ film from the substrate by dipping it into water with no polymer support or chemical treatment.

REFERENCES

11. Kim, C. -J. *et al.* Chiral atomically thin films. *Nat. Nanotech.* **11**, 520 (2016).
16. Liu, K. *et al.* Evolution of interlayer coupling in twisted molybdenum disulfide bilayers. *Nat. Commun.* **5**, 4966 (2014).
20. Kang, K. *et al.* High-mobility three-atom-thick semiconducting films with wafer-scale homogeneity. *Nature* **520**, 656 (2015).
24. Simmons, J. G. Generalized formula for the electric tunnel effect between similar electrodes separated by a thin insulating film. *J. Appl. Phys.* **34**, 1793 (1963).
25. Kang, J., Tongay, S., Zhou, J., Li, J., Wu J. Band offsets and heterostructures of two-dimensional semiconductors. *Appl. Phys. Lett.* **102**, 012111 (2013).
29. Gurarlsan, A. *et al.* Surface-energy-assisted perfect transfer of centimeter-scale monolayer and few-layer MoS₂ films onto arbitrary substrates. *ACS Nano* **8**, 11522 (2014).
31. Muller, D. A. *et al.* Atomic-scale chemical imaging of composition and bonding by aberration-corrected microscopy. *Science* **319**, 1073 (2008).
32. Cueva, P., Hovden, R., Mundy, J. A., Xin, H. L., Muller, D. A. Data processing for atomic resolution electron energy loss spectroscopy. *Microsc. Microanal.* **18**, 667 (2012).
33. Amani, M. *et al.* Near-unity photoluminescence quantum yield in MoS₂. *Science* **350**, 1065 (2015).
34. van Der Zande, A. M. *et al.* Tailoring the electronic structure in bilayer molybdenum disulfide via interlayer twist. *Nano Lett.* **14**, 3869 (2014).
35. Lee, C. *et al.* Anomalous lattice vibrations of single- and few-layer MoS₂. *ACS Nano* **4**, 2695 (2010).
36. Mak, K. F. *et al.* Atomically thin MoS₂: a new direct-gap semiconductor. *Phys. Rev. Lett.* **105**, 136805 (2010).
37. Zheng, S. *et al.* Coupling and interlayer exciton in twist-stacked WS₂ bilayers. *Adv. Opt. Mat.* **3**, 1600 (2015).
38. Tongay, S. *et al.* Tuning interlayer coupling in large-area heterostructures with CVD-grown MoS₂ and WS₂ monolayers. *Nano Lett.* **14**, 3185 (2014).
39. Hong, X. *et al.* Ultrafast charge transfer in atomically thin MoS₂/WS₂ heterostructures. *Nat. Nanotech.* **9**, 682 (2014).
40. Xu, Y., Schoonen M. A. A. The absolute energy positions of conduction and valence bands of selected semiconducting minerals. *American Mineralogist* **85**, 543 (2000).
41. Shi, H., Pan, H., Zhang, Y., Yakobson, B. I. Quasiparticle band structures and optical properties of strained monolayer MoS₂ and WS₂. *Phys. Rev. B.* **87**, 155304 (2013).
42. Molina-Sánchez, A., Wirtz, L. Phonons in single-layer and few-layer MoS₂ and WS₂. *Phys. Rev. B.* **84**, 155413 (2011).
43. Chen, X. *et al.* Probing the electron states and metal-insulator transition mechanisms in molybdenum disulphide vertical heterostructures. *Nat. Commun.* **6**, 6088 (2015).